The roles of equatorial trapped waves and internal inertia-gravity waves in driving the quasi-biennial oscillation. Part I: zonal mean wave forcing

Yoshio Kawatani
Japan Agency for Marine-Earth Science and Technology, Yokohama, Japan

Kaoru Sato
Department of Earth and Planetary Science, Graduate School of Science, University of Tokyo, Tokyo, Japan

Timothy J. Dunkerton
Northwest Research Associates, Redmond, WA, USA

Shingo Watanabe
Japan Agency for Marine-Earth Science and Technology, Yokohama, Japan

Saburo Miyahara
Department of Earth and Planetary Sciences, Graduate School of Sciences, Kyushu University, Fukuoka, Japan

Masaaki Takahashi
Center for Climate System Research, University of Tokyo, Kashiwa, Japan

Submitted on 5th June 2009
Revised on 14th September 2009
Revised on 6th November 2009
J. Atmos. Sci.

---

[1]*Corresponding author address:* Yoshio Kawatani, Japan Agency for Marine-Earth Science and Technology, Yokohama, 236-0001, Japan
E-mail: yoskawatani@jamstec.go.jp

Abstract

The roles of equatorial trapped waves (EQWs) and internal inertia-gravity waves in driving the quasi-biennial oscillation (QBO) are investigated using a high-resolution atmospheric general circulation model with T213L256 resolution (60-km horizontal and 300-m vertical resolution) integrated for 3 years. The model, which does not use a gravity-wave drag parameterization, simulates a QBO. Although the simulated QBO has a shorter period than that of the real atmosphere, its amplitudes and structure in the lower stratosphere are fairly realistic. The zonal wavenumber / frequency spectra of simulated outgoing longwave radiation represent realistic signals of convectively coupled EQWs. Clear signals of EQWs are also seen in the stratospheric wind components. In the eastward wind shear of the QBO, eastward EQWs including Kelvin waves contribute up to ~25–50% to the driving of the QBO. The peaks of eastward wave forcing associated with EQWs and internal inertia-gravity waves occur at nearly the same time at the same altitude. On the other hand, westward EQWs contribute up to ~10% to driving the QBO during the weak westward wind phase but make almost zero contribution during the relatively strong westward wind phase. Extratropical Rossby waves propagating into the equatorial region contribute ~10–25%, whereas internal inertia-gravity waves with zonal wavelength $\leq$~1000 km are the main contributors to the westward wind shear phase of the simulated QBO.

1. Introduction

A large-scale zonal-mean zonal wind oscillation called the quasi-biennial oscillation (QBO) exists in the equatorial lower stratosphere. Previous studies have reported that the QBO is driven by atmospheric waves through wave-mean flow interaction (cf. Baldwin *et al.* 2001). Lindzen and Holton (1968) proposed the first successful theory of the QBO. Using a two-dimensional model, they showed that critical-level absorption of a broad spectrum of vertically propagating gravity waves drives the QBO. Holton and Lindzen (1972) refined the work of Lindzen and Holton (1968) by using a one-dimensional model. They proposed that the QBO is driven by eastward-propagating Kelvin waves with zonal wavenumber 1 and a 15-day period and westward-propagating mixed Rossby-gravity (MRG) waves with zonal wavenumber 4 and a 4-day period, which were discovered from radiosonde observations (Wallace and Kousky 1968; Yanai and Maruyama 1966).

Holton and Lindzen (1972) did not consider the mean upward motion existing in the equatorial lower stratosphere, which has an estimated magnitude of approximately 0.3 mm s^{-1} (e.g., Mote *et al.* 1996, 1998; Schoeberl *et al.* 2008). On the other hand, the downward-propagating speed of the QBO is approximately 0.5 mm s^{-1}. The equatorial mean upward motion makes the QBO phase move upward, whereas the wave forcing makes the QBO phase move downward. Therefore, the wave forcing should have a stronger effect than the equatorial upward flow (Dunkerton 1991). Thus, when realistic equatorial upwelling is included in models, the required total wave flux for the QBO is two to four times larger than that of observed large-scale Kelvin and MRG waves (Takahashi and Boville 1992; Baldwin *et al.* 2001 and references therein).

Recently, Ern and Preusse (2009) estimated the wave forcing associated with Kelvin waves with zonal wavenumber 1-6 using Sounding of the Atmosphere using Broadband Emission Radiometry (SABER) data, They indicated that the contribution of Kelvin waves is only 20-30 % of the expected total wave forcing during eastward wind shear phase of the QBO. A broad spectrum of waves exists in the tropics, and many of these waves contribute to driving the QBO (Baldwin *et al.* 2001). A combination of Kelvin, MRG, other equatorial trapped waves (EQWs), and internal inertia-gravity waves (for simplicity, referred to hereafter as "internal gravity waves") is believed to provide most of the momentum flux needed to drive the QBO (Dunkerton 1997; Sato and Dunkerton 1997). The relatively small temporal and spatial scales of internal gravity waves preclude comprehensive investigations of wave forcing over a wide geographic range using only observational data.

Atmospheric general circulation models (AGCMs) are effective tools with which to study the roles of atmospheric waves in driving the QBO (Takahashi 1996, 1999; Horinouchi and Yoden 1998; Giorgetta *et al.* 2002, 2006; Hamilton *et al.* 1999, 2001; Shibata and Deushi 2005a, b; Kawatani *et al.* 2005). Takahashi (1996) achieved the first realistic simulation of the QBO-like oscillation in an AGCM (for simplicity, we shall hereafter refer to the QBO-like oscillation as the QBO). He used an AGCM with T21 truncation (horizontal resolution of approximately 600 km) that included vertical grid spacing of approximately 500 m so that wave-mean flow interactions between equatorial winds and explicitly resolved waves could be represented. However, in order to obtain the QBO, he had to reduce the horizontal diffusion coefficients to increase the power of waves in the stratosphere.

Horinouchi and Yoden (1998) simulated the QBO using an aquaplanet T42 AGCM with uniform sea surface temperature (SST). They conducted a thorough wave analysis and reported that the gravest symmetric gravity modes [i.e., eastward propagating Kelvin waves and westward propagating n = 1 gravity waves, where n is the order of the solution of Eq. (8), shown later] account for approximately half of the transport and deposition of the zonal momentum contributing to the QBO. They also indicated that zonal wavenumber / frequency spectra of simulated cumulus heating in the troposphere show clear spectral peaks associated with Kelvin and n = 1 gravity waves. Giorgetta *et al.* (2006) simulated the QBO using an AGCM with T42 resolution that included the gravity wave drag parameterization by Hines (1997). They showed that resolved large-scale waves are particularly important for reproducing the eastward wind phase, whereas parameterized gravity wave drag is more important for the westward wind phase. Studies using higher resolution AGCMs (Hamilton *et al.* 1999, 2001; Kawatani *et al.* 2005) also reported the importance of internal gravity waves in driving the QBO. However, those studies did not investigate the relative contributions of EQWs and internal gravity waves in driving the QBO.

Recently, we conducted experiments with a much higher resolution AGCM (T213L256; from the surface to ~85 km; see details in the next section) to investigate interesting phenomena related to middle-atmosphere dynamics (Watanabe *et al.* 2008; Tomikawa *et al.* 2008; Watanabe *et al.* 2009; Sato *et al.* 2009). The time integration was made over 3 years using physical quantities sampled every 1 hour. The purpose of this study is to clarify the relative contributions of EQWs and internal gravity waves in driving the QBO in the 10°S–10°N mean field using outputs from the high-resolution

AGCM. The companion paper, Kawatani *et al.* (2010), investigates the three-dimensional distribution of wave forcing.

The paper is arranged as follows. Section 2 describes the model. Section 3 examines aspects of the simulated QBO. Section 4 describes equatorial trapped waves. Section 5 discusses the relative role of equatorial trapped waves and internal inertia-gravity waves in driving the QBO. Section 6 presents the QBO simulated with T106 resolution. Section 7 summarizes the study and provides concluding remarks.

2. Model description

The model used is based on the atmospheric component of version 3.2 of the Model for Interdisciplinary Research on Climate (MIROC), a coupled atmosphere–ocean GCM developed by the Center for Climate System Research/National Institute for Environmental Studies/Frontier Research Center for Global Change (CCSR/NIES/FRCGC; K-1 Model Developers 2004). The atmospheric GCM has been referred to in previous studies as the CCSR/NIES AGCM and CCSR/NIES/FRCGC AGCM. This model has been used for studies of the QBO and/or atmospheric gravity waves (Takahashi 1996, 1999; Sato *et al.* 1999; Kawatani *et al.* 2003, 2004, 2005, 2009; Watanabe and Takahashi 2005; Watanabe *et al.* 2006, 2008, 2009; Watanabe 2008). The equations used in the model are primitive equations on a sphere (i.e., the model is hydrostatic). The model has a horizontal resolution of T213 spectral truncation, which corresponds to a grid interval of approximately 60 km in the tropics (0.5625°). Two hundred fifty-six vertical layers are represented (L256), and the top boundary is at 0.01

hPa (~85 km). The vertical resolution is set to 300 m from the upper troposphere through the whole middle atmosphere.

The cumulus parameterization is based on that reported by Arakawa and Schubert (1974). In the original Arakawa–Schubert scheme, convective precipitation characteristically becomes more frequent and weaker as the horizontal resolution of the GCM increases. To prevent this problem, a relative humidity-limit method is incorporated into the cumulus convection scheme (Emori *et al.* 2001). If the ratio between the vertical integration of the specific humidity and that of the saturation specific humidity from the bottom to the top of a cloud is less than a critical value (here, 0.72), the cloud mass flux is set to zero (see Emori *et al.* 2001 for further details). This method results in the suppression of overly frequent precipitation and the generation of organized convective precipitation. Suzuki *et al*. (2006) showed that incorporation of this method in the CCSR/NIES/FRCGC AGCM substantially improves the representation of convectively coupled EQWs. The present model also reproduces realistic short-term variability of convective clouds, such as westward propagating cloud clusters with horizontal scales of several hundred to several thousand kilometers and periods of 1–2 days, and eastward propagating super cloud cluster-like structures with zonal phase speeds of ~15 m s^{-1} (cf. Nakazawa 1988).

The Mellor and Yamada (1982) level-2 closure scheme is used for eddy vertical diffusion parameterization. A dry convective adjustment is applied to eliminate convective instability that is not suppressed by the vertical diffusion parameterization. Fourth-order horizontal diffusion is used, and the e-folding time for the smallest resolved wave is 0.9 days. Note that a standard value of the horizontal coefficient is used in the

model (i.e., there is no need to reduce the horizontal diffusion coefficient). Monthly mean climatological SST and realistic topography are used as the bottom boundary conditions. This experiment included no gravity-wave drag parameterization. Thus, gravity waves are spontaneously generated in the model. The data for wave analysis were sampled every hour as hourly averages for 3 years.

The set of parameters (e.g., horizontal and vertical diffusion, cumulus parameterization) employed in the present simulation were obtained by conducting several sensitivity experiments. To arrive at suitable parameters, attention was primarily paid to obtaining realistic gravity wave amplitudes in the lower stratosphere (e.g., Sato and Dunkerton 1997; Sato *et al.* 2003). More detailed model explanations have been provided by Watanabe *et al.* (2008).

3. Aspects of the simulated QBO

3.1. Simulated QBO and zonal wave forcing with different horizontal scales

The model successfully simulated the observed features of the atmospheric general circulation. The position and strength of the subtropical jet were realistic in both hemispheres. Realistic separation between the subtropical jet and the polar night jet was also simulated. More detailed general aspects of the model have been described by Watanabe *et al.* (2008). In this section, aspects of the simulated QBO and zonal wave forcing with different horizontal scales are discussed.

The Eliassen–Palm flux (EP-flux), which is widely used to analyze wave propagation and zonal wave forcing in the meridional plane of zonal-mean zonal wind, is defined as follows in spherical and log-pressure coordinates (Andrews *et al.* 1987):

$$F^{(\phi)} = \rho_0 a \cos\phi \left(\bar{u}_z \overline{v'\theta'} / \bar{\theta}_z - \overline{u'v'} \right), \tag{1}$$

$$F^{(z)} = \rho_0 a \cos\phi \left\{ \left[f - (a\cos\phi)^{-1} \left(\bar{u}\cos\phi \right)_\phi \right] \overline{v'\theta'} / \bar{\theta}_z - \overline{u'w'} \right\}, \tag{2}$$

$$\nabla \cdot \mathbf{F} = \left(a\cos\phi \right)^{-1} \partial / \partial\phi \left(F^{(\phi)} \cos\phi \right) + \partial F^{(z)} / \partial z , \tag{3}$$

with the zonally averaged momentum equation expressed as

$$\bar{u}_t = \bar{v}^* \left[f - \left(a\cos\phi \right)^{-1} \left(\bar{u}\cos\phi \right)_\phi \right] - \bar{w}^* \bar{u}_z + \left(\rho_0 a \cos\phi \right)^{-1} \nabla \cdot \mathbf{F} + \overline{X} \ . \tag{4}$$

In the above equations, ρ_0, a, ϕ, z, u, v, w, θ, and f are the log-pressure height dependent density, the mean radius of the Earth, latitude, log-pressure height, zonal wind, meridional wind, vertical wind, potential temperature, and Coriolis parameter ($f \equiv 2\Omega\sin\phi$, where Ω is the rotation rate of the Earth), respectively. The subscripts ϕ, z, and t denote a meridional, vertical, and time derivative, respectively. The mean residual circulations of the meridional and vertical components are expressed by $\bar{v}^*$ and $\bar{w}^*$. Eastward and westward wave forcing correspond to EP-flux divergence and convergence (i.e., $\nabla \cdot \mathbf{F} > 0$ and $\nabla \cdot \mathbf{F} < 0$), respectively.

Figure 1a shows a time–height cross section of monthly mean zonal-mean zonal wind and the EP-flux divergence due to all wave components at 10°S–10°N for 3 years. An obvious QBO with a period of approximately 15 months can be seen. The maximum speed of the westward wind at 30 hPa is approximately -25 m s^{-1}, and that of the eastward wind is 15 m s^{-1} over the equator [a time–height cross section of zonal-mean zonal wind over the equator is shown in Fig. 7 of Watanabe *et al.* (2008)]. The simulated amplitude of the QBO is consistent with that in the real atmosphere (Naujokat 1986). The westward and eastward winds extend down to approximately 80–100 hPa in the model. As noted by

Fig.1

Dunkerton (2000), wave forcings must be sufficiently strong to bring the QBO down to the lowermost stratosphere above the tropical tropopause, where the largest atmospheric density in the altitude range of the QBO occurs. Therefore, correct downward penetration of the QBO is a stringent test of model realism.

The meridional widths of both eastward and westward wind phases are similar to those in the 40-yr European Centre for Medium-Range Weather Forecasts (ECMWF) Re-Analysis (ERA-40; Uppala *et al.* 2005) data (see Fig. 5 of Giorgetta *et al.* 2006) (not shown). The eastward wind phase is narrower in latitude than the westward wind phase. Onset of the eastward wind phase occurs first at the equator, whereas onset of the westward wind phase happens more evenly over the equatorial latitudes (Hamilton 1984; Dunkerton and Delisi 1985). The stratopause semi-annual oscillation (SSAO) is also well simulated.

Red and blue colors show eastward and westward wave forcings, which correspond well to the eastward wind shear ($\partial \bar{u}/\partial z > 0$, where z denotes altitude) and the westward wind shear ($\partial \bar{u}/\partial z < 0$), respectively. These results indicate that spontaneously generated waves resolved in the model certainly drive the QBO. Maximum eastward wave forcing is located around the 0 m s^{-1} line of the zonal-mean zonal wind. In contrast, the maximum westward wave forcing occurs around the ~-10 m s^{-1} line of the zonal wind. The absolute values of eastward and westward wave forcing are comparable. The downward propagation speed of the eastward wind shear is faster than that of the westward wind shear, but the difference is not as obvious as in the real atmosphere (discussed in part II of this paper). Eastward shear-zone descent is faster in the model (~1.6 km per month) than in the observations (~1 km per month), and an even larger

difference is found in the westward shear-zone descent. The relationship between wave forcing and the vertical zonal wind shear is also clear at altitudes of the SSAO, indicating that the SSAO is also driven by resolved waves. Detailed analysis of the SSAO will be examined in another paper.

To investigate what horizontal scales of waves contribute to driving the QBO, the EP-flux divergences associated with zonal wavenumber (s) bands $1 \le s \le 11$, $12 \le s \le 42$, $43 \le s \le 106$, and $107 \le s \le 213$ were calculated. Each zonal wavenumber band corresponds to zonal wavelengths λ_x of $\sim 3600 \le \lambda_x \le 40{,}000$ km, $\sim 950 \le \lambda_x \le 3300$ km, $\sim 380 \le \lambda_x \le 930$ km, and $\sim 180 \le \lambda_x \le 370$ km over the equator. Waves with $1 \le s \le 11$ include Kelvin waves, MRG waves, other EQWs, large-scale gravity waves, tides, and extratropical Rossby waves propagating into the equatorial region. Waves with $s \le 42$ could be explicitly resolved by the lower resolution AGCM used for past QBO simulation (the T42 AGCM used by Horinouchi and Yoden 1998; Takahashi 1999; and Giorgetta *et al.* 2006), and waves with $s \le 106$ could be resolved by the higher resolution AGCM (T106 AGCM by Kawatani *et al.* 2005, 2009). Hamilton *et al.* (1999, 2001) studied the QBO using AGCMs, including for $s \ge 106$; however, for the N270L40 AGCM (N denotes the number of grid rows between the pole and equator), the highest resolutions of their simulations were only for several months.

Figures 1b–d show the time variation of the EP-flux divergence due to $1 \le s \le 11$, $12 \le s \le 42$, $43 \le s \le 106$, and $107 \le s \le 213$ at 15, 30, and 45 hPa for 3 years (10°S–10°N average). First, zonal wave forcing at 30 hPa is discussed (Fig. 1c). In the eastward wind shear phase, eastward wave forcing due to $1 \le s \le 11$ is strongest, and eastward wave forcings due to $12 \le s \le 42$, $43 \le s \le 106$, and $107 \le s \le 213$ are comparable. Wave

scales contributing to the westward wind shear of the QBO differ greatly. Westward wave forcing due to $1 \leq s \leq 11$ makes a much smaller contribution than do the other wave forcings. Westward wave forcing due to $42 \leq s \leq 213$ ($\lambda x \leq$ ~1000 km) contributes greatly to driving the westward wind shear phase of the QBO. These results are consistent with those of a T42 AGCM study by Giorgetta *et al.* (2006); resolved large-scale waves are important for the eastward wind shear phase, whereas parameterized gravity wave drag plays crucial roles in the westward wind phase.

The relative contribution of eastward wave forcing due to $1 \leq s \leq 11$ becomes smaller at 15 hPa than at 30 hPa and 45 hPa, but wave scales contributing to the eastward wind shear phase of the QBO do not differ greatly by altitude. On the other hand, the wave scales contributing to the westward wind shear show much dependence on height. At 15 hPa, westward wave forcing due to $1 \leq s \leq 11$ is comparable to that due to other wave forcings (see section 5 for more detailed discussion). On the other hand, westward wave forcing due to $107 \leq s \leq 213$ plays significant roles at 45 hPa. Section 6 discusses the roles of waves with $107 \leq s \leq 213$ in driving the westward wind shear phase of the QBO.

Next, to investigate the zonal phase velocity distribution relative to the ground (C_x) of the EP-flux, the zonal wavenumber-frequency distribution of the EP-flux is calculated as follows:

$$F^{(\phi)}(s,\omega) = \rho_0 a \cos\phi \left(\bar{u}_z \, \hat{v}(s,\omega) \hat{\theta}^*(s,\omega) / \bar{\theta}_z - \hat{u}(s,\omega) \hat{v}^*(s,\omega) \right), \tag{5}$$

$$F^{(z)}(s,\omega) = \rho_0 a \cos\phi \, \mathrm{Re}\left\{ \left[f - (a\cos\phi)^{-1} \left(\bar{u} \cos\phi \right)_\phi \right] \hat{v}(s,\omega) \hat{\theta}^*(s,\omega) / \bar{\theta}_z - \hat{u}(s,\omega) \hat{w}^*(s,\omega) \right\}, \tag{6}$$

where an asterisk denotes the complex conjugate, and $\hat{u}$, $\hat{v}$, $\hat{w}$, and $\hat{\theta}$ are the Fourier coefficients of zonal, meridional, and vertical wind, and the potential temperature (cf. Horinouchi *et al.* 2003), respectively. The EP-flux divergence is then calculated following Eq. (3).

Figure 2 shows the zonal wavenumber / frequency spectra of the $F^{(z)}$ and EP-flux divergence during the eastward wind shear phase of the QBO at 45–25 hPa in July of the first year (left panels) and the westward wind shear phase at 35–20 hPa in January of the second year (right panels). The altitude range was selected based on the distribution of strong wave forcing (see Fig. 1a). Solid lines depict C_x. Positive zonal wavenumbers correspond to positive C_x (eastward propagation), and negative zonal wavenumbers correspond to negative C_x (westward propagation).

Fig.2

In the eastward wind shear, $F^{(z)}$ is mostly distributed in the range of $C_x \geq 2$ m s^{-1} in positive zonal wavenumbers and $C_x \leq -15$ m s^{-1} in negative zonal wavenumbers (Fig. 2a). The spectra of the EP-flux divergence indicate that most eastward wave forcing occurs in the range of 2 m s^{-1} $\leq C_x \leq$ 20 m s^{-1} (Fig. 2c). The EP-flux divergence with values $\geq\sim$1 x 10^{-9} m s^{-1} wavenumber^{-1} cpd^{-1} (cpd: cycles per day) is distributed up to zonal wavenumber 140. On the other hand, in the westward wind shear, $F^{(z)}$ is distributed in the range of $C_x \geq 10$ m s^{-1} in positive zonal wavenumbers and $C_x \leq -5$ m s^{-1} in negative zonal wavenumbers (Fig. 2b). The westward wave forcing with values $\leq$ -1 x 10^{-9} m s^{-1} wavenumber^{-1} cpd^{-1} is distributed in the range of -30 m s^{-1} $\leq C_x \leq$ -5 m s^{-1} up to zonal wavenumber 180 in the westward wind shear phase (Fig. 2d).

These results demonstrate that westward wave forcing with smaller horizontal scale and faster C_x dominates in the westward wind shear phase compared to the eastward

wave forcing in the eastward wind shear phase. The spectral distributions also suggest that waves with continuous phase-velocity distributions contribute to the QBO, as reported previlusly (Lindzen and Holton 1968; Dunkerton 1997; Horinouchi and Yoden 1998; Hamilton *et al.* 2001; Giorgetta *et al.* 2002).

3.2. Tropical upwelling due to the Brewer-Dobson circulation

The simulated period of the oscillation is about half that of the QBO in the real atmosphere. Two explanations for the shorter period are possible: one is underestimation of mean ascent motion in the equatorial lower stratosphere that slows the downward phase propagation of the QBO, and the other is overestimation of the wave forcing that drives the QBO.

To quantitatively investigate mean ascent in the equatorial lower stratosphere, the residual vertical velocity is estimated in the transformed Eulerian mean (TEM) equation as follows (Andrews *et al.* 1987):

$$\overline{w}^{*} = \overline{w} + (a\cos\phi)^{-1}(\cos\phi\overline{v'\theta'}/\overline{\theta}_{z})_{\phi}. \qquad (7)$$

Figure 3 shows the time–height cross section of $\overline{w}^{*}$ averaged from 10°N–10°S. The vertical profile of averaged $\overline{w}^{*}$ for two cycles of the QBO (i.e., from January of the first year to June of the third year) is shown in the right panel. The $\overline{w}^{*}$ becomes positive and large during the westward wind shear but becomes negative during the relatively strong eastward wind shear above ~40 hPa. The secondary circulation associated with the QBO is ascent in the westward wind shear and descent in the eastward wind shear (Plumb and Bell 1982). The negative $\overline{w}^{*}$ in the eastward wind shear would result from secondary

Fig.3

circulation associated with the QBO's being stronger than the climatological ascent motion in the tropics.

The averaged $\overline{w}^*$ is approximately 0.33 mm s^{-1} near 80 hPa, decreases to 0.16 mm s^{-1} at ~50 hPa, and then rises to 0.24 mm s^{-1} at ~15 hPa. The averaged $\overline{w}^*$ from 70 to 15 hPa is ~0.18 mm s^{-1}. In ERA-40 data, negative $\overline{w}^*$ also appears above ~30 hPa during eastward wind shear. The climatological $\overline{w}^*$ in ERA-40 data for the period 1979–2001 is ~0.33 mm s^{-1} from 70 to 15 hPa. Mote *et al.* (1996) estimated a vertical velocity of 0.2–0.4 mm s^{-1} between 16 and 32 km (between 100 and 10 hPa) from water vapor tape recorder signals. Schoeberl *et al.* (2008) estimated that $\overline{w}^*$ is approximately 0.4 mm s^{-1} near 18 km (~76 hPa) and decreases to 0.3 mm s^{-1} at 21 km (~50 hPa). Therefore, the mean $\overline{w}^*$ in the model used here might be approximately half that in the real atmosphere, resulting in the shorter period of simulated QBO. Roughly speaking, we expect that if upwelling in the model were doubled, the rate of eastward shear-zone descent would be reduced by about 0.5 km per month, bringer the total descent rate into better agreement with observations. It is trickier to estimate the effect of increased upwelling on westward shear-zone descent, which might conceivably reach approximately zero at certain times of the year, lengthening the descent time significantly. In any case, it is clear that the period of the simulated QBO could be increased with realistic upwelling without any substantial reduction of *in situ* wave forcing.

The model used here overestimates the strength of stratospheric eastward wind in the extratropical winter hemisphere (Watanabe *et al.* 2008), which implies underestimation of wave forcing due to gravity waves and/or Rossby waves in the mid- to

high latitudes. Underestimated wave forcing in the mid- to high latitudes would result in underestimation of Brewer–Dobson circulation and thus weaker $\overline{w}^*$ in the tropics. Exploration of the detailed relationship between the period of the QBO and wave forcing in the mid- to high latitudes is beyond the scope of the present study. Further analysis of the zonal momentum budget of Rossby waves and gravity waves in the extra tropics is currently underway.

Using an AGCM with T42L90 resolution, Giorgetta *et al.* (2006) simulated a realistic period of the QBO and realistic $\overline{w}^*$. Wave forcing of resolved waves plus forcing due to parameterized gravity wave drag in their study (see their Fig. 10) was comparable to that in the our study (Fig. 1a). Thus, wave forcing in the model used here may not have been largely overestimated. Detailed validation of wave momentum flux is discussed in part II of this study.

Another possible reason for the short period of the QBO is that climatological ozone is used in this experiment. Shibata and Deushi (2005b) investigated the radiative effect of ozone on the QBO using an AGCM with coupled chemistry. In their interactive ozone run, the periods of the QBO were ~1.5–1.8 times longer than were those in the non-interactive run, although a clear mechanism for the ozone effect was not mentioned in their study.

4. Equatorial trapped waves

The analysis in the previous section could not distinguish the relative contributions of EQWs and internal gravity waves to driving the QBO. Therefore, separate wave components are examined in more detail in this section.

Because convection is the strongest source of waves in the tropics, it is important to investigate how realistically convective activities are simulated. Convectively coupled EQWs could be the source of EQWs propagating into the stratosphere (Wheeler *et al.* 2000; Kawatani *et al.* 2009; Kiladis *et al.* 2009). To evaluate how well the model used in this study simulates convectively coupled EQWs, space–time spectral analysis of outgoing longwave radiation (OLR) was performed using daily data from the National Oceanic and Atmospheric Administration (NOAA) and the model output. Three years of data were used for the spectral calculation. NOAA OLR data from 1979 to 1981 were used when neither an El Niño nor a La Niña event occurred, based on the criteria for those events defined by the Japan Meteorological Agency. The procedure is briefly outlined below; further details have been provided by Wheeler and Kiladis (1999), Lin *et al.* (2006), and Kawatani *et al.* (2009). Grid data $D(\phi)$ as a function of latitude ϕ can be expressed as the sum of symmetric $DS(\phi)$ and antisymmetric $DA(\phi)$ components, with $DS(\phi) = [D(\phi) + D(-\phi)]/2$ and $DA(\phi) = [D(\phi) - D(-\phi)]/2$. The OLR data were decomposed into symmetric and antisymmetric components. Space–time spectra were then calculated for successive overlapping segments of data and averaged. Here, 128 days, with 78 days of overlap between each segment, were calculated.

Figures 4a and b show zonal wavenumber / frequency spectra obtained by averaging the powers of symmetric and antisymmetric components [i.e., (DS + DA)/2] of the NOAA OLR and the model (10°S–10°N average). Note that erroneous spectral peaks from artifacts of the satellite sampling in NOAA OLR data are not plotted (cf. Wheeler and Kiladis 1999). The spectra are red in both wavenumber and frequency, but differences between eastward and westward components are obvious. Although the

Fig.4

model slightly overestimates (underestimates) westward (eastward) components, it relatively well simulates the spectral distributions. Lin *et al.* (2006) also reported that the present model was one of the best models available worldwide for realistically simulating spectral power at periods of ≤6 days. The well-simulated spectrum of OLR in this study would result in better simulation of equatorial wave activity in the stratosphere (Horinouchi *et al.* 2003; Kawatani *et al.* 2009). On the other hand, the model underestimates the Madden–Julian Oscillation (MJO), although disturbances associated with the MJO do not directly contribute to driving the simulated QBO (not shown). It is generally difficult to simulate realistic MJO in present GCMs (Lin *et al.* 2006).

The dispersion relation of EQW modes in shallow-water equations on an equatorial beta plane is expressed as follows (Matsuno 1966):

$$\frac{m^2\hat{\omega}^2}{N^2} - k^2 - \frac{\beta k}{\hat{\omega}} = (2n+1)\frac{\beta \mid m \mid}{N}, \quad n = 0,1,2,\ldots., \tag{8}$$

where $\hat{\omega}$, k, and n are the intrinsic frequency, zonal wavenumber, and order of the solution, respectively. The solutions of wave modes have structures trapped at the equator. For Kelvin waves (n = -1), the dispersion relation is the same as that for internal gravity waves with zero meridional wavelengths as follows:

$$\frac{\hat{\omega}^2}{k^2} = gh_e, \tag{9}$$

where h_e is the equivalent depth, which is connected with the vertical wavenumber m as follows:

$$m^2 = \left(\frac{N^2}{gh_e} - \frac{1}{4H^2} \right), \tag{10}$$

where H is the scale height, and the vertical wavelength λ_z is calculated from the vertical wavenumber as $\lambda_z = 2\pi / m$ (see Andrews *et al.* 1987 for detailed derivations of the above equations).

Figures 4c–f show the zonal wavenumber / frequency spectra of symmetric and antisymmetric components of OLR divided by the background spectra appearing in the NOAA OLR data and the model (10°S–10°N average). The "background spectra" were calculated by averaging the powers of DA and DS and smoothing with a 1–2–1 filter in frequency and wavenumber. The dispersion curves of the odd (n = -1, 1) and even modes (n = 0, 2) of equatorial waves for the five equivalent depths of 8, 12, 25, 50, and 90 m are superposed under the assumption of zero background wind. The frequency spectral width is 1/128 cpd, and the minimum resolvable period is 0.5 cpd (2 days). In the areas corresponding to the dispersion curves, clear signals of Kelvin waves and n = 1 equatorial Rossby waves are present in symmetric components, whereas MRG waves and n = 0 eastward inertia-gravity waves (hereafter, eastward- and westward-propagating inertia-gravity waves are referred to as EIGWs and WIGWs, respectively) are obvious in antisymmetric components in both the observation and model results.

Figures 5a–d show the zonal wavenumber / frequency spectra of the symmetric and antisymmetric components of zonal and meridional wind averaged from 82 to 35 hPa in July for the first year (10°S–10°N average). Because the spectra of wind components do not have a red noise-like background spectrum, normalization using the background spectra was not applied to the symmetric and asymmetric spectra. The dispersion curves of EQWs for the three equivalent depths of 8, 90, and 500 m are superposed under the assumption of zero background wind.

Fig.5

For zonally propagating waves, the intrinsic frequency $\hat{\omega}$ is written as follows:

$$\hat{\omega} = \omega - k\bar{u}\,, \tag{11}$$

where ω and $\bar{u}$ are the ground-based frequency and background zonal wind, respectively. Note that the ground-based frequency ω and zonal wavenumber k are conserved in the vertical, assuming that the background flow does not change in time or longitude, respectively, although the intrinsic frequency $\hat{\omega}$ and vertical wavenumber m vary according to the Doppler (11) and dispersion relationships. The distribution of zonal wavenumber / frequency spectra of momentum fluxes would be changed only if a wave were to undergo critical-level filtering and/or wave dissipation (Ern *et al.* 2008 and references therein).

Clear signals of Kelvin waves, MRG waves, n = 0 EIGWs, and n = 1 equatorial Rossby waves can be seen in Figs. 5a–d. The peaks corresponding to n = 1 EIGWs/WIGWs become much clearer in spectra of meridional wind (Fig. 5c) in which Kelvin waves do not appear under zero background wind (Matsuno 1966). Note that the spectral distributions are relatively similar to those of OLR in the range of $8 \leq h_e \leq 90$ m (Figs. 4c–f), which suggests a possible connection between stratospheric EQWs and tropospheric wave sources of convectively coupled EQWs (Kawatani *et al.* 2009). Other spectral peaks with periods of approximately 1 day and a wide zonal wavenumber range in both symmetric and antisymmetric components are also present. These wavenumbers may correspond to the tide and/or internal gravity waves generated by the diurnal cycle of convection (Kawatani *et al.* 2003, 2009).

To extract EQW components, an adequate equatorial wave filter is needed. The characteristics of the frequency / the zonal wavenumber spectra are helpful in creating an

equatorial wave filter. First we must define the range of the zonal wavenumber and the minimum and maximum h_e of EQWs. The spectral mass of EQWs is found within $1 \leq s \leq 11$ (Figs. 5a–d). Following previous studies, the wave components with relatively long horizontal wavelengths ($s \leq 11$; $\lambda_x \geq$ ~3600 km) are regarded as EQWs in the present study.

When zonally propagating internal gravity waves meet critical levels, the vertical wavelength (i.e., proportional to h_e) becomes small. In this study, the minimum h_e was set to 2 m, which corresponds to the vertical wavelength of ~1.1 km under $N^2 = 6 \times 10^{-4}$ s^{-2}. Because the vertical resolution of the model is 300 m, these waves could be resolved. Maximum h_e was set to 90 m, following previous studies (e.g., Ern *et al.* 2008; Alexander *et al.* 2008; Kawatani *et al.* 2009). In the case of Kelvin waves, h_e = 90 m corresponds to C_x ~30 m, which is larger than the amplitude of the QBO in the eastward wind phase. Ern *et al.* (2008) reported that an EQW with $h_e \leq 90$ m was mainly modulated by the QBO and that higher equivalent depths ($90 \leq h_e \leq 2000$ m) showed less pronounced variation due to the QBO but more variation due to the SSAO.

Figures 5e and f show the spectral domain extracted by the equatorial wave filter. Dispersion curves with h_e of 2 and 90 m were drawn under the assumption of zero background wind. The zonal wind is small near the equatorial lowest stratosphere (Fig. 1a). The minimum period was set to 1.1 day (~0.9 cpd) to avoid including waves with a period of 1 day. In calculating the zonal wave forcing associated with EQWs, overlaps between Kelvin waves and n = 1 EIGWs and between n = 0 EIGWs and n = 2 EIGWs were avoided. That is, a Kelvin / n = 1 EIGW and n = 0 / n = 2 EIGW wave filter was

applied. Fluctuations with $s \geq 12$ are analyzed as internal gravity waves. The wave filter was applied to temperature, wind, and geopotential height.

Although the extracted spectral ranges are decided by equivalent depths, they actually correspond to the specific ranges of the frequency and zonal wave number domains. Zonal wave forcing associated with EQWs can be investigated using this equatorial wave filter because the ground-based frequency ω and zonal wavenumber k of a wave do not change unless the waves propagate in a mean flow that varies with time or longitude, respectively (Ern *et al.* 2008; Kawatani *et al.* 2009).

The longitude-time cross sections of the filtered temperature disturbances showed that global-scale $s = 1$, 2 Kelvin waves dominate with periods of ~10–20 days and amplitude of ~3 K (not shown). On the other hand, the simulated MRG waves have amplitude of ~1.2 K with periods of ~3–6 days and $3 \leq s \leq 5$. These results are consistent with those from the Constellation Observing System for Meteorology, Ionosphere, and Climate (COSMIC) GPS radio occultation (RO) data (Alexander *et al.* 2008) and SABER data (Ern *et al.* 2008). Furthermore, the spatial structures of the extracted EQWs in the stratosphere generally agree with those derived theoretically by Matsuno (1966) (not shown).

5. The relative role of equatorial trapped waves and internal inertia-gravity waves in driving the QBO

The relative role of EQWs and internal gravity waves in driving the QBO at the 10°S–10°N mean field is discussed in this section using the EP-flux divergence [Eq. (3)]. Figure 6 shows time–height cross sections of the EP-flux divergence due to Kelvin waves

Fig.6

/ n = 1 EIGWs, MRG waves, n = 0 / n = 2 EIGWs, and n = 1 plus n = 2 WIGWs at 10°S–10°N. Note that the color interval depicting Kelvin waves / n = 1 EIGWs is five times greater than that of the other EQWs. The connection of the equatorial Rossby waves between the upper troposphere and stratosphere is not very clear (not shown). The vertically propagating responses of convectively coupled equatorial Rossby waves are confined to within a few kilometers of the wave generation (see discussions by Wheeler *et al.* 2000 and references therein). Therefore, we do not include a figure showing equatorial Rossby waves here. Zonal wave forcing due to eastward EQWs (left panels) corresponds well to the eastward wind shear phase of the QBO. Most eastward wave forcing lies around the 0 m s^{-1} line of zonal-mean zonal wind. Eastward wave forcing due to the odd mode of eastward EQWs (i.e., Kelvin waves / n = 1 EIGWs) is much larger than that due to the even mode of eastward EQWs (i.e., n = 0 / n = 2 EIGWs). For example, in July of the first year, the EP-flux divergence due to all wave components is ~4.8 x 10^{-1} m s^{-1} day^{-1} around 35 hPa (Fig. 1a), whereas those divergences due to the odd and even modes are ~1.7 x 10^{-1} m s^{-1} day^{-1} and 0.4 x 10^{-1} m s^{-1} day^{-1}, respectively. The contribution is ~35% for the odd mode and 8% for the even mode. Consequently, eastward-propagating EQWs contribute ~43% of the total wave forcing around 35 hPa during this time period.

Zonal wave forcing due to westward EQWs (right panels) generally corresponds well to the westward wind shear phase of the QBO. Around 20–40 hPa, westward wave forcing due to MRG waves is stronger than that due to n = 1 plus n = 2 WIGWs. In contrast to eastward EQWs, the westward EQW contribution to driving the QBO is small. For example, in January of the second year, the EP-flux divergence due to all waves is

~4.0 x 10^{-1} m s^{-1} day^{-1} around 28 hPa (Fig. 1a). On the other hand, the wave forcing due to MRG waves is ~0.3 x 10^{-1} m s^{-1} day^{-1}, and the sum of total wave forcing due to westward EQWs is ~0.4 x 10^{-1} m s^{-1} day^{-1}, representing only ~10% of total westward wave forcing. As mentioned in section 1, some previous studies reported that the wave forcing due to MRG waves is small. An additional important point is that westward EQWs (i.e., the sum of MRG waves, n = 1 / n = 2 WIGWs, and equatorial Rossby waves) also make small contributions to driving the QBO during the westward wind shear phase.

Figures 7a and 7b show the time variation of zonal-mean zonal wind, its tendency [$\overline{u}_t$; the left side of Eq. (4)], the EP-flux divergence due to all wave components, eastward EQWs, westward EQWs, internal gravity waves, and forcing due to residual circulation [the first plus second terms of the right side of Eq. (4)] at 30 hPa averaged from 10°S to 10°S. The tendency of the zonal-mean zonal wind proceeds to the variation of the zonal-mean zonal wind. Generally, forcing due to residual circulation is opposite to the total wave forcing, and its absolute value is smaller than that of total wave forcing.

Fig.7

In the eastward wind shear phase, eastward wave forcing due to eastward EQWs is up to ~2.5 x 10^{-1} m s^{-1} day^{-1}, whereas that by internal gravity waves is up to ~5.0 x 10^{-1} m s^{-1} day^{-1}. The peaks of both eastward wave forcings occur at nearly the same time. The eastward EQWs during three peaks of strong eastward wave forcing (i.e., June of the first year, September of the second year, and October of the third year) contribute ~53%, 27%, and 43% of total wave forcing, respectively.

Westward wave forcing due to internal gravity waves is up to ~-5.0 x 10^{-1} m s^{-1} day^{-1}, and that due to westward EQWs is up to ~-0.5 x 10^{-1} m s^{-1} day^{-1}. Westward EQWs contribute up to ~10% to QBO driving during the weak westward wind phase, but their

contribution is nearly zero during the relatively strong westward wind phase of the QBO (compare the blue line of Fig. 7a and the green line of Fig. 7b). Consequently, internal gravity waves play crucial roles in driving the QBO in the westward wind shear phase of the simulated QBO.

The EP-flux divergence due to $s \leq 11$ but without extracted EQW components was also calculated to investigate large-scale wave forcing other than by the extracted EQWs (i.e., extratropical Rossby waves, large-scale gravity waves, tides, and EQWs with $h_e \geq 90$ m; hereafter called "large-scale non-EQWs"). Large-scale non-EQW components were determined as waves which do not satisfy the dispersion curves of EQWs with $2 \leq h_e \leq 90$ m [i.e., not in the hatched spectral domain in Figs. 5e, f with $s \leq 11$ and periods >1.1 cpd with $s \leq 11$ (not drawn in Figs. 5e, f)]. Figure 7c shows the time variation of the EP-flux divergence of all components due to $s \leq 11$ and that due to large-scale non-EQWs (10°S–10°N average). The wave forcing due to eastward and westward EQWs is drawn again in Fig. 7c. Note that the range of the ordinate axis is different from that in Figs. 7a and 7b. During the eastward wind shear phase, the contribution of large-scale non-EQWs is small. On the other hand, during the westward wind shear phase, westward wave forcing due to large-scale non-EQWs is comparable to that due to westward EQWs at this altitude. During the westward wind shear phase, most of the westward wave forcing associated with large-scale non-EQWs is due to Rossby waves propagating from the winter hemisphere, as suggested by the EP-flux due to large-scale non-EQWs (not shown).

Figure 8 is the same as Fig. 7, but for 15 hPa and 45 hPa. General features are not very different from those at 30 hPa. However, it is clear that non-EQWs (i.e., Fig.8

extratropical Rossby waves) play more important roles at higher altitude during the westward wind shear phase (Fig. 8e). For example, in January of the third year, when the phase of the QBO changes from eastward to westward wind around 15 hPa (see blue line in Fig. 8a), extratropical Rossby waves contribute ~24% to the westward wind shear phase of the QBO. Extratropical Rossby waves make a much larger contribution to the westward wind shear phase in the upper level than in the lower level of the QBO (see yellow lines in Figs. 7c, 8e, 8f) (cf. Ortland 1997; O'Sullivan 1997). On the other hand, at 45 hPa, internal gravity waves (red line) explain most of total zonal wave forcing (black line) during the westward wind shear (Fig. 8d). As shown in Fig. 1d, these internal gravity waves mainly result from waves with $107 \leq s \leq 213$. Table 1 summarizes the relative contributions of waves to the QBO.

6. The QBO Simulated with T106 resolution

In this section, the roles of internal gravity waves with $107 \leq s \leq 213$ in the QBO in the lower stratosphere are discussed. The realistic lowermost level of the westward wind phase of the QBO (~80 hPa) was well simulated in the T213L256 AGCM (Fig. 1a), whereas it was not simulated by the same AGCM with T106L60 resolution (1.125° horizontal grid; Kawatani *et al.* 2005, 2009) or by the Geophysical Fluid Dynamics Laboratory (GFDL) "SKIHI" AGCM with N90L80 resolution (1.2°–1° resolution on a longitude–latitude grid; Hamilton *et al.* 2001). Because the vertical resolution of T106L60 is about 550 m in the stratosphere, the comparison between the T213L256 and T106L60 AGCM simulations includes the effect of different vertical resolutions. Therefore, an experiment using T106 with the same vertical resolution of 300 m was

conducted. The top boundary was set at about 1 hPa (~50 km; i.e., L152 levels), which is different from T213L256. However, a T106L152 AGCM would be sufficient for investigating the reproducibly of the QBO in the lower stratosphere.

Figure 9 is the same as Fig. 1a, but for T106L152 for 3 years. The absolute values of EP-flux divergence are smaller than those in T213L256, but they are comparable to those with $1 \leq s \leq 106$ in the T213L256 AGCM (not shown). The $\overline{w}^*$ in the T106L152 run is approximately half that in the real atmosphere (not shown) as in T213L256 (Fig. 3). As a result, the QBO with a period of approximately 2 years is seen. The most important result in Fig. 9 is that westward wave forcing around 45 hPa is much smaller than that in T213 (Fig. 1a), and the lowermost level of the westward wind phase of the QBO is located around 40–50 hPa. These results strongly support the conclusion that very small-scale internal gravity waves ($\lambda_x \leq$ ~370 km) play crucial roles in the westward wind shear phase of the QBO in the lower stratosphere.

7. Summary and concluding remarks

This study has investigated the roles of EQWs and internal gravity waves in driving the QBO using an AGCM with resolution of T213L256 integrated for 3 years. The model, which does not use a gravity wave drag parameterization, simulates QBO (QBO-like oscillation) and SSAO. The simulated QBO has a shorter period than the QBO of the real atmosphere, which would result from underestimation of mean ascent motions ($\overline{w}^*$) in the tropics. The amplitude and lowermost levels of the QBO are realistically simulated.

The model well simulated convectively coupled EQWs, which are important for representing EQW activity in the stratosphere (Kawatani *et al.* 2009). The choice and tuning of cumulus convective parameterization could affect the results. The EP-flux divergences of all wave components indicate that spontaneously generated waves resolved in the model drive the QBO. The zonal wavenumber / frequency spectra of EP-flux divergence illustrate that wave forcing with smaller horizontal scale and faster C_x dominated in the westward wind shear phase compared to that in the eastward wind shear phase.

EQWs with equivalent depths in the range of 2–90 m from the n = -1 mode to n = 2 mode were extracted separately in the range of $s \leq 11$. Fluctuations with $s \geq 12$ are analyzed as internal gravity waves. In the eastward wind shear of the QBO, eastward EQWs contribute up to ~25–50% to driving the QBO. The peaks of eastward wave forcing associated with EQWs and internal gravity waves occur at nearly the same time at the same altitude. On the other hand, westward-propagating EQWs (i.e., MRG waves, n = 1 and n = 2 WIGWs, and equatorial Rossby waves) contribute up to ~10% to driving the QBO during the weak westward wind phase, but their contribution is nearly zero during the relatively strong westward wind phase. Extratropical Rossby waves from the winter hemisphere contribute ~10–25% in the westward wind shear phase, and their contribution is larger in the upper level of the QBO. Internal gravity waves with zonal wavelength less than ~1000 km provide the main contribution to the westward wind shear phase. Comparison between T213 and T106 AGCMs supports the conclusion that internal gravity waves with $107 \leq s \leq 213$ play crucial roles in the westward wind shear in the lower stratosphere.

Horinouchi and Yoden (1998) indicated that symmetric gravity wave modes (Kelvin waves and n = 1 WIGWs) account for approximately half of the transport and deposition of zonal momentum contributing to the QBO. The results of the present study generally agree with their findings for Kelvin waves but not for n = 1 WIGWs. The precipitation of their GCM was largest over the equator and smallest between 10° and 20° (see Fig. 1 of their paper), which is a preferable condition for generating a more symmetric n = 1 mode of EQWs. In addition, Horinouchi and Yoden (1998) considered n = 1 WIGWs with $1 \leq s \leq 30$ in a T42 model, whereas we considered EQWs with $1 \leq s \leq 11$ in a T213 model. The spectral domain of n = 1 WIGWs includes most of the westward waves of the symmetric mode when including zonal wavenumbers of $s \geq 12$ (see Fig. 5e; extending the dispersion curves of n = 1 WIGWs to $s \geq 12$). The use of an aquaplanet AGCM with uniform SST by Horinouchi and Yoden (1998) may also have contributed to the difference between their and our results.

Convectively coupled n = 1 WIGWs are underestimated in our model (Fig. 4), which might result in less activity of n = 1 WIGWs in the stratosphere. However, spectral analysis reveals that waves with $\lambda_x \leq \sim 1000$ km contribute substantially to driving the westward wind shear phase of the simulated QBO, which could be shown using a much higher resolution model. Thus, it could be inferred that westward-propagating EQWs make small contributions to driving the QBO.

The amplitude and periods of simulated Kelvin waves and MRG waves are comparable to those found by recent satellite-based observation studies (Ern *et al.* 2008; Alexander *et al.* 2008). We have also confirmed that small-scale internal gravity waves are well simulated in comparison to limited *in situ* observations (e.g., Sato and Dunkerton

1997; Sato *et al.* 2003; detailed explanation is provided in Part II of this study. See also Watanabe et al. 2008 and Sato et al. 2009). However, we do not have enough observations to verify the realism of the simulated wave forcing, especially for small-scale internal gravity waves. The fine vertical resolution of 300 m sufficiently resolves the majority of observed gravity waves, but T213 horizontal resolution is still insufficient to resolve very small-scale gravity waves ($\lambda_x \leq 180$ km). The roles of very small-scale internal gravity waves in driving the QBO should be investigated using an ultra-high resolution model.

In this paper, we have focused on investigating zonal-mean wave forcing in the field of 10°N–10°S. Recent satellite and modeling studies have indicated that wave activity depends greatly on zonal direction (Alexander *et al.* 2008; Ern *et al.* 2008; Kawatani *et al.* 2009). The three-dimensional distribution of wave forcing is discussed in part II of this paper.

Acknowledgments.

The authors thank to Profs. I. Hirota, T. Tsuda, Drs. T. Imamura, Y. Tomikawa, K. Miyazaki and S. P. Alexander for valuable suggestions on this study. We express our gratitude to Dr. K.K Tung for editing the manuscript and two anonymous reviewers for constructive comments on the original manuscripts. This work is a contribution to the Innovative Program of Climate Change Projection of the 21st Century, MEXT, Japan. The simulation was conducted using the Earth Simulator. The GFD-DENNOU Library and GrADS were used to draw the figures. This work was supported by a Grant-in-Aid for Scientific Research (19204047) from the Ministry of Education, Culture, Sports, Science and Technology, Japan, and also by a Grant for Young Scientists (B) (20740280) from the Japan Society for the Promotion of Science.

References

Alexander, S. P., T. Tsuda, Y. Kawatani, and M. Takahashi, 2008: Global distribution of atmospheric waves in the equatorial upper troposphere and lower stratosphere: COSMIC observations of wave mean flow interactions, *J. Geophys. Res*., **113**, D24115, doi:10.1029/2008JD010039.

Andrews, D. G.., J. R. Holton, and C. B. Leovy, 1987: Middle Atmosphere Dynamics, *Academic Press*, 489 pp.

Arakawa, A., and W. H. Schubert, 1974: Interactions of cumulus cloud ensemble with the large-scale environment. Part I, *J. Atmos. Sci*., **46**, 661–685.

Baldwin, M. P., L. J. Gray, T. J. Dunkerton, K. Hamilton, P. H. Haynes, W. J. Randel, J. R. Holton, M. J. Alexander, I. Hirota, T. Horinouchi, D. B. A. Jones, J. S. Kinnersley, C. Marquardt, K. Sato, and M. Takahashi, 2001: The quasi-biennial oscillation, *Rev. of Geophys.*, **39**, 179–229.

Dunkerton, T. J., 1991: Nonlinear propagation of zonal winds in an atmosphere with Newtonian cooling and equatorial wavedriving, *J. Atmos. Sci*., **48**, 236–263.

Dunkerton, T. J., 1997: The role of gravity waves in the quasi-biennial oscillation, *J. Geophys. Res.*, **102**, 26,053–26,076.

Dunkerton, T. J., 2000: Midwinter deceleration of the subtropical mesospheric jet and interannual variability of the high-latitude flow in UKMO analyses, *J. Atmos. Sci*., **57**, 3838–3855.

Dunkerton, T. J., and D. P. Delisi, 1985: Climatology of the equatorial lower stratosphere, *J. Atmos. Sci*., **42**, 376–396.

Emori, S., T. Nozawa, A. Numaguti, and I. Uno, 2001: Importance of cumulus parameterization for precipitation simulation over East Asia in June, *J. Meteor. Soc. Japan*, **79**, 939–947.

Ern, M., and P. Preusse, 2009: Quantification of the contribution of equatorial Kelvin waves to the QBO wind reversal in the stratosphere, *Geophys. Res. Lett*., **36**, L21801, doi:10.1029/2009GL040493.

Ern, M., P. Preusse, M. Krebsbach, M. G. Mlynczak, and J. M. Russell, III, 2008: Equatorial wave analysis from SABER and ECMWF temperatures, *Atmos. Chem. Phys.*, **8**, 845–869.

Giorgetta, M. A., E. Manzini, and E. Roechner, 2002: Forcing of the quasi-biennial oscillation from a broad spectrum of atmospheric waves, *Geophysic. Res. Lett*., **29**, 1245, doi:10.1029/2002GL014756.

Giorgetta, M. A., E. Manzini, E. Roechner, M. Esch, and L. Bengtsson, 2006: Climatology and forcing of the quasi-biennial oscillation in the MAECHAM5 model, *J. Climate*, **19**, 3882–3901.

Hamilton, K., 1984: Mean wind evolution through the quasi-biennial cycle of the tropical lower stratosphere, *J. Atmos. Sci*., **41**, 2113–2125.

Hamilton, K., R. J. Wilson, and R. Hemler, 1999: Atmosphere simulated with high vertical and horizontal resolution versions of a GCM: Improvement in the cold pole bias and generation of a QBO-like oscillation in the tropics, *J. Atmos. Sci.*, **56**, 3829–3846.

Hamilton, K., R. J. Wilson, and R. Hemler, 2001: Spontaneous stratospheric QBO-like oscillations simulated by the GFDLSKYHI general circulation model, *J. Atmos. Sci.*, **58**, 3271–3292.

Hines, C. O., 1997: Doppler-spread parameterization of gravity wave momentum deposition in the middle atmosphere, 2, Broad and quasi-monochromatic spectra, and implementation, *J. Atmos. Terr. Phys.*, **59**, 387–400.

Holton, J. R., and R. S. Lindzen, 1972: An updated theory for the quasi-biennial cycle of the tropical stratosphere, *J. Atmos. Sci*., **29**, 1076–1080.

Horinouchi, T., and S. Yoden, 1998: Wave-mean flow interaction associated with a QBO-like oscillation simulated in a simplified GCM, *J. Atmos. Sci*., **55**, 502–526.

Horinouchi, T., S. Pawson, K. Shibata, U. Langematz, E. Manzini, M. A. Giorgetta, F. Sassi, R. J. Wilson, K. Hamilton, J. de Grandpre, and A. A. Scaife, 2003: Tropical cumulus convection and upward-propagating waves in middle-atmospheric GCMs, *J. Atmos. Sci*., **60**, 2765–2782.

K-1 model developers, K-1 Coupled GCM (MIROC) Description, 2004: K-1 Technical Report, 1, 1–34 pp, University of Tokyo, Tokyo, Japan.

Kawatani, Y., S. K. Dhaka, M. Takahashi, and T. Tsuda, 2003: Large potential energy of gravity waves over a smooth surface with little convection, *Geophys. Res. Lett.*, **30**(8), 1438, doi:10.1029/2003GL016960.

Kawatani, Y., M. Takahashi, and T. Tokioka, 2004: Gravity waves around the subtropical jet of the southern winter in an atmospheric general circulation model, *Geophys. Res. Lett*., **31**, L22109, doi:10.1029/2004GL020794.

Kawatani, Y., K. Tsuji, and M. Takahashi, 2005: Zonally non-uniform distribution of equatorial gravity waves in an atmospheric general circulation model, *Geophys. Res. Lett.*, **32**, L23815, doi:10.1029/2005GL024068.

Kawatani, Y., M. Takahashi, K. Sato, S. P. Alexander, and T. Tsuda, 2009: Global distribution of atmospheric waves in the equatorial upper troposphere and lower stratosphere: AGCM simulation of sources and propagation, *J. Geophys. Res*, **114**, D01102, doi:10.1029/2008JD010374.

Kawatani, Y., K. Sato, T. J. Dunkerton, S. Watanabe, S. Miyahara, and M. Takahashi, 2010: The roles of equatorial trapped waves and internal inertia-gravity waves in driving the quasi-biennial oscillation. Part II: Three-dimensional distribution of wave forcing, *submitted to J. Atmos. Sci*.

Kiladis, G. N., M. C. Wheeler, P. T. Haertel, K. H. Straub, P. E. Roundy, 2009: Convectively coupled equatorial waves, *Rev. Geophys.*, **47**, RG2003, doi:10.1029/2008RG000266.

Lin, J.-L., G. N. Kiladis, B. E. Mapes, K. M. Weickmann, K. R. Sperber, W. Lin, M. C. Wheeler, S. D. Schubert, A. Del Genio, L. J. Donner, S. Emori, J.-F. Gueremy, F. Hourdin, P. J. Rasch, E. Roeckner, and J. F. Scinocca, 2006: Tropical intraseasonal variability in 14 IPCC AR4 climate models. Part I: Convective signals, *J. Climate*, **19**, 2665–2690, doi:10.1175/JCLI3735.1

Lindzen, R. S., and J. R. Holton, 1968: A theory of the quasi-biennial oscillation, *J. Atmos. Sci*., **25**, 1095–1107.

Matsuno, T., 1966: Quasi-geostrophic motions in the equatorial area, *J. Meteor. Soc. Japan*, **44**, 25–43.

Mellor, G. L., and T. Yamada, 1982: Development of a turbulence closure model for geostrophic fluid problems, *Rev. Geophys.*, **20**, 851–875.

Mote, P. W., K. H. Rosenlof, M. E. Mcintyre, E. S. Carr, J. C. Gille, J. R. Holton, J. S. Kinnersley, H. C. Pumphrey, J. M. Russell, and J. W. Waters, 1996: An atmospheric tape recorder: The imprint of tropical tropopause temperatures on stratospheric water vapor, *J. Geophys. Res*., **101**, 3989–4006.

Mote, P. W., T. J. Dunkerton, M. E. Mclntyre, E. A. Ray, P. H. Haynes, and J. M. Russell III, 1998: Vertical velocity, vertical diffusion, and dilution by midlatitude air in the tropical lower stratosphere, *J. Geophys. Res*., **103**(D8), 8651–8666.

Nakazawa, T., 1988: Tropical super clusters within intraseasonal variations over the western Pacific, *J. Meteor. Soc. Japan*, **66**, 823–839.

Naujokat, B., 1986: An update of the observed quasi-biennial oscillation of the stratospheric wind over the tropics, *J. Atmos. Sci.*, **43**, 1873–1877.

Ortland, D. A., 1997: Rossby wave propagation into the tropical stratosphere observed by the High Resolution Doppler Imager, *Geophys. Res. Lett.*, **24**, 1999–2002.

O'Sullivan, D., 1997: Interaction of extratropical Rossby waves with eastward wind quasi-biennial oscillation winds, *J. Geophys. Res*., **102**, 19,461–19,469.

Plumb, R. A., and R. C. Bell, 1982: A model of the quasi-biennial oscillation on an equatorial beta-plane, *Q. J. R. Meteorol. Soc*., **108**, 335–352.

Sato, K., and T. J. Dunkerton, 1997: Estimates of momentum flux associated with equatorial Kelvin and gravity waves, *J. Geophys. Res*., **102**, 26,247–26,261.

Sato, K., T. Kumakura, and M. Takahashi, 1999: Gravity waves appearing in a high resolution GCM simulation, *J. Atmos. Sci.*, **56**, 1005–1018.

Sato, K., M. Yamamori, S. Ogino, N. Takahashi, Y. Tomikawa, and T. Yamanouchi, 2003: A meridional scan of the stratospheric gravity wave field over the ocean in 2001 (MeSSO2001), *J. Geophys. Res*., **108**, 4491, doi:10.1029/2002JD003219.

Sato, K., S. Watanabe, Y. Kawatani, Y. Tomikawa, K. Miyazaki, and M. Takahashi, 2009: On the origins of mesospheric gravity waves, *Geophys. Res. Lett*., **36**, L19801, doi:10.1029/2009GL039908.

Schoeberl, M. R., A. R. Douglass, R. S. Stolarski, S. Pawson, S. E. Strahan, and W. Read, 2008: Comparison of lower stratospheric tropical mean vertical velocities, *J. Geophys. Res.*, **113**, D24109, doi:10.1029/2008JD010221.

Shibata, K. and M. Deushi, 2005a: Partitioning between resolved wave forcing and unresolved gravity wave forcing to the quasi-biennial oscillation as revealed with a coupled chemistry–climate model, *Geophys. Res. Lett*., **32**, L12820, doi:10.1029/2005GL022885.

Shibata, K. and M. Deushi, 2005b: Radiative effect of ozone on the quasi-biennial oscillation in the equatorial stratosphere, *Geophys. Res. Lett*., **32**, L24802, doi:10.1029/2005GL023433.

Suzuki, T., Y. N. Takayabu, and S. Emori (2006), Coupling mechanisms between equatorial waves and cumulus convection in an AGCM, *Dyn. Atmos. Oceans*, **42**, 81–106, doi:10.1016/j.dynatmoce.2006.02.004.

Takahashi, M., 1996: Simulation of the stratospheric quasi-biennial oscillation using a general circulation model, *Geophys. Res. Lett*., **23**, 661–664.

Takahashi, M., 1999: Simulation of the quasi-biennial oscillation in a general circulation model, *Geophys. Res. Lett*., **26**, 1307–1310.

Takahashi, M., and B. A. Boville, 1992: A three-dimensional simulation of the equatorial quasi-biennial oscillation, *J. Atmos. Sci*., **49**, 1020–1035.

Tomikawa, Y. K. Sato, S. Watanabe, Y. Kawatani, K. Miyazaki, and M. Takahashi, 2008: Wintertime temperature maximum at the subtropical stratopause in a T213L256 GCM, *J. Geophys. Res*., **113**, D17117, 2008JD009786.

Uppala S. M., P. W. Kallberg, A. J. Simmons, U. Andrae, V. D. Bechtold, M. Fiorino, J. K. Gibson, J. Haseler, A. Hernandez, G. A. Kelly, X. Li, K. Onogi, S. Saarinen, N. Sokka, R. P. Allan, E. Andersson, K. Arpe, M. A. Balmaseda, A. C. M. Beljaars, L. Van De Berg, J. Bidlot, N. Bormann, S. Caires, F. Chevallier, A. Dethof, M. Dragosavac, M. Fisher, M. Fuentes, S. Hagemann, E. Holm, B. J. Hoskins, L. Isaksen, P. A. E. M. Janssen, R. Jenne, A. P. McNally, J. F. Mahfouf, J. J. Morcrette, N. A. Rayner, R. W. Saunders, P. Simon, A. Sterl, K. E. Trenberth, A. Untch, D. Vasiljevic, P. Viterbo, and J. Woollen, 2005: The ERA-40 re-analysis, *Quart. J. Roy. Meteor. Soc*., **131**, 2961–3012.

Wallace, J. M., and V. E. Kousky, 1968: Observation evidence of Kelvin waves in the tropical stratosphere, *J. Atmos. Sci.*, **25**, 900–907.

Watanabe, S., 2008: Constraints on a non-orographic gravity wave drag parameterization using a gravity wave resolving general circulation model, *SOLA*, **4**, 61–64.

Watanabe, S., and M. Takahashi, 2005: Kelvin waves and ozone Kelvin waves in the quasi-biennial oscillation and semiannual oscillation: A simulation by a high-resolution chemistry-coupled general circulation model, *J. Geophys. Res*., **110**, D18303, doi:10.1029/2004JD005424.

Watanabe, S., K. Sato, and M. Takahashi, 2006: A general circulation model study of orographic gravity waves over Antarctica excited by katabatic winds, *J. Geophys. Res*., **111**, D18104, doi:10.1029/2005JD006851.

Watanabe, S., Y. Kawatani, Y. Tomikawa, K. Miyazaki, M. Takahashi, and K. Sato, 2008: General aspects of a T213L256 middle atmosphere general circulation model, *J. Geophys. Res*., **113**, D12110, doi:10.1029/2008JD010026.

Watanabe, S., Y. Tomikawa, K. Sato, Y. Kawatani, K. Miyazaki and M. Takahashi, 2009: Simulation of the eastward 4-day wave in the Antarctic winter mesosphere using a gravity wave resolving general circulation model, *J. Geophys. Res*, **114**, D16111, doi:10.1029/2008JD011636.

Wheeler, M., and G. N. Kiladis, 1999: Convectively coupled equatorial waves: Analysis of clouds and temperature in the wavenumber-frequency domain, *J. Atmos. Sci.*, **56**, 374–399.

Wheeler, M., G. N. Kiladis, and P. J. Webster, 2000: Large-scale dynamical fields associated with convectively coupled equatorial waves, *J. Atmos. Sci.*, **57**, 613–640.

Yanai, M., and T. Maruyama, 1966: Stratospheric wave disturbances propagating over the equatorial Pacific, *J. Meteor. Soc. Japan*, **44**, 291–294.

List of Table and Figures

Table 1. Relative contributions of zonal wave forcing during the eastward wind and westward wind shear phases of the QBO at 10°S–10°N.

Fig. 1. (a) Time–height cross section of monthly mean zonal-mean zonal wind (contour) and monthly mean EP-flux divergence (colors) at 10°S–10°N. Red and blue colors correspond to eastward and westward wave forcing, respectively. The contour intervals are 5 m s^{-1}. The solid and dashed lines correspond to eastward and westward winds, respectively. Time variation of monthly mean EP-flux divergence due to $1 \leq s \leq 11$ (blue), $12 \leq s \leq 42$ (green), $43 \leq s \leq 106$ (yellow), and $107 \leq s \leq 213$ (red) at (b) 15 hPa, (c) 30 hPa, and (d) 45 hPa (10°S–10°N average).

Fig. 2. Zonal wavenumber-frequency spectra of (a, b) the vertical component of EP-flux (Kg s^{-2} wavenumber^{-1} cpd^{-1}) and (c, d) EP-flux divergence (m s^{-2} wavenumber^{-1} cpd^{-1}) during (a, c) the eastward wind shear phase of the QBO in July at 45–25 hPa and (b, d) the westward wind shear phase of the QBO in January at 35–20 hPa. Solid lines show the zonal phase velocity C_x relative to the ground. Positive (negative) zonal wavenumber corresponds to positive (negative) C_x. The vertical component of EP-flux and EP-flux divergence are multiplied by 30 and 1 x 10^9, respectively. The color scale is logarithmic.

Fig. 3. Time–height cross section of the monthly mean vertical component of residual circulation $\overline{w}^*$ (white and gray shading) and zonal wind (contour) averaged from 10°N–10°S. Eastward and westward winds are represented by solid and dashed lines,

respectively, with intervals of 5 m s^{-1}. Positive values are shaded and negative values are dotted, with intervals of 0.1 mm s^{-1}. Vertical profiles of averaged $\overline{w}^*$ for two cycles of the QBO are shown in the right panel with labels of log-pressure height.

Fig. 4. (a, b) Zonal wavenumber / frequency spectra obtained by averaging the powers of symmetric and antisymmetric components of OLR averaged from 10°N to 10°S. Spectral units are $\log_{10}(W^2\ m^{-4}$ wavenumber^{-1} cpd$^{-1})$. (c, d) Symmetric and (e, f) antisymmetric components divided by the background spectra. Left and right panels present results from NOAA OLR data and the model data, respectively. These results are from 3-year average data. The shading interval is 0.2; values ≥ 1.1 are shown for (c–f). Dispersion curves indicate the odd and even modes of equatorial waves for the five equivalent depths of 8, 12, 25, 50, and 90 m. The frequency spectral width is 1/128 cpd.

Fig. 5. Zonal wavenumber / frequency spectra of the (a, d) symmetric and (b, c) antisymmetric components of (a, b) zonal wind and (c, d) meridional wind at 82–35 hPa during July of the first year (10°N–10°S average). The spectral unit is $\log_{10}(m^2\ s^{-2}$ wavenumber^{-1} cpd$^{-1})$. The contour interval is 0.3 $m^2\ s^{-2}$ wavenumber^{-1} cpd^{-1}. Note that the ranges of shading differ between the zonal wind and meridional wind components; values ≥ -2.1 and ≥ -2.4 are shaded for (a, b) and (c, d), respectively. Contour lines show the dispersion curves of each EQW with equivalent depths of 8, 90, and 500 m. Application of the equatorial wave filter to (e) odd and (f) even modes of EQWs. Superposed are the dispersion curves of each EQW for two equivalent depths of 2 and 90 m. Hatched areas between the two lines are the filtering range.

Fig. 6. Time–height cross section of monthly mean EP-flux divergence (colors) due to (a) Kelvin waves / n = 1 EIGWs, (b) MRG waves, (c) n = 0 / n = 2 EIGWs, and (d) n = 1 plus n = 2 WIGWs with equivalent depths from 2 to 90 m at 10°S–10°N. The color interval is 2.5 x 10^{-2} m s^{-1} day^{-1} for (a) and 0.5 x 10^{-2} m s^{-1} day^{-1} for (b–d). The contour interval is 5 m s^{-1} for the zonal-mean zonal wind.

Fig. 7. Time variation of (a) zonal-mean zonal wind and its tendency; (b) monthly mean EP-flux divergence due to all waves (black), eastward EQWs (blue), westward EQWs (green), internal gravity waves (red), and forcing due to residual circulation (yellow) at 30 hPa averaged from 10°S to 10°S; (c) EP-flux divergence due to $s \leq 11$ (black), eastward EQWs (blue), westward EQWs (green), and large-scale non-EQWs (yellow), respectively. Note that the range of the ordinate axis of (c) is different from that of (a) and (b).

Fig.8. Same as Figure 7, but for at (a, c, e) 15 hPa and (b, d, f) 45 hPa.

Fig. 9. Same as Figure 1a, but showing the result of the T106L152 AGCM integrated for 3 years.

Table 1

Table 1. Relative contributions of zonal wave forcing during the eastward wind and westward wind shear phases of the QBO at 10°S–10°N.

	EQWs	internal inertia-gravity waves	Rossby waves from the winter hemisphere
eastward wind shear	~25–50%	~50–75%	
westward wind shear	up to ~10% during weak westward wind phase	$\lambda x \leq$~1000 km main wave forcing	~10–25%; larger in the upper level

Fig.1

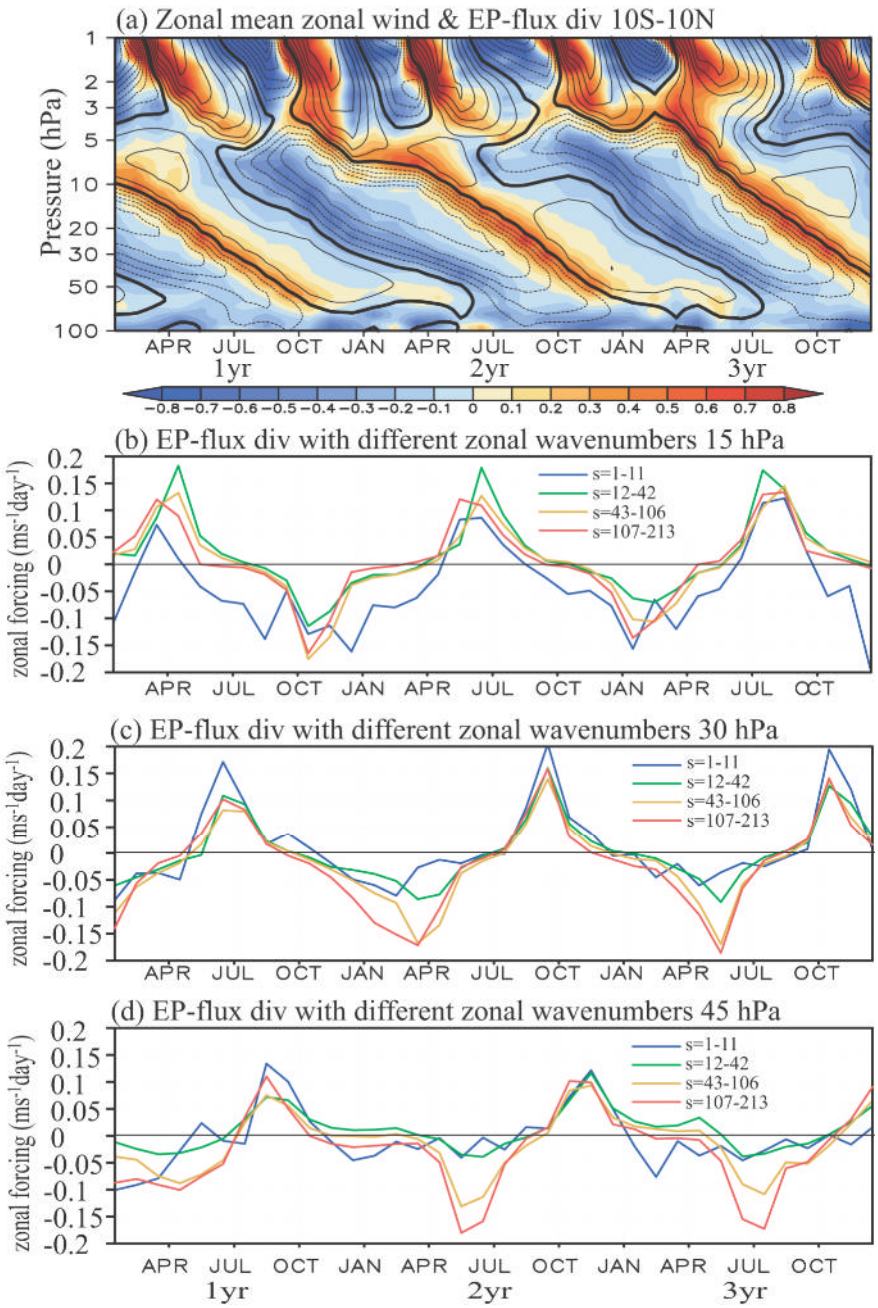

Fig. 1. (a) Time–height cross section of monthly mean zonal-mean zonal wind (contour) and monthly mean EP-flux divergence (colors) at 10°S–10°N. Red and blue colors correspond to eastward and westward wave forcing, respectively. The contour intervals are 5 m s^{-1}. The solid and dashed lines correspond to eastward and westward winds, respectively. Time variation of monthly mean EP-flux divergence due to $1 \le s \le 11$ (blue), $12 \le s \le 42$ (green), $43 \le s \le 106$ (yellow), and $107 \le s \le 213$ (red) at (b) 15 hPa, (c) 30 hPa, and (d) 45 hPa (10°S–10°N average).

Fig. 2

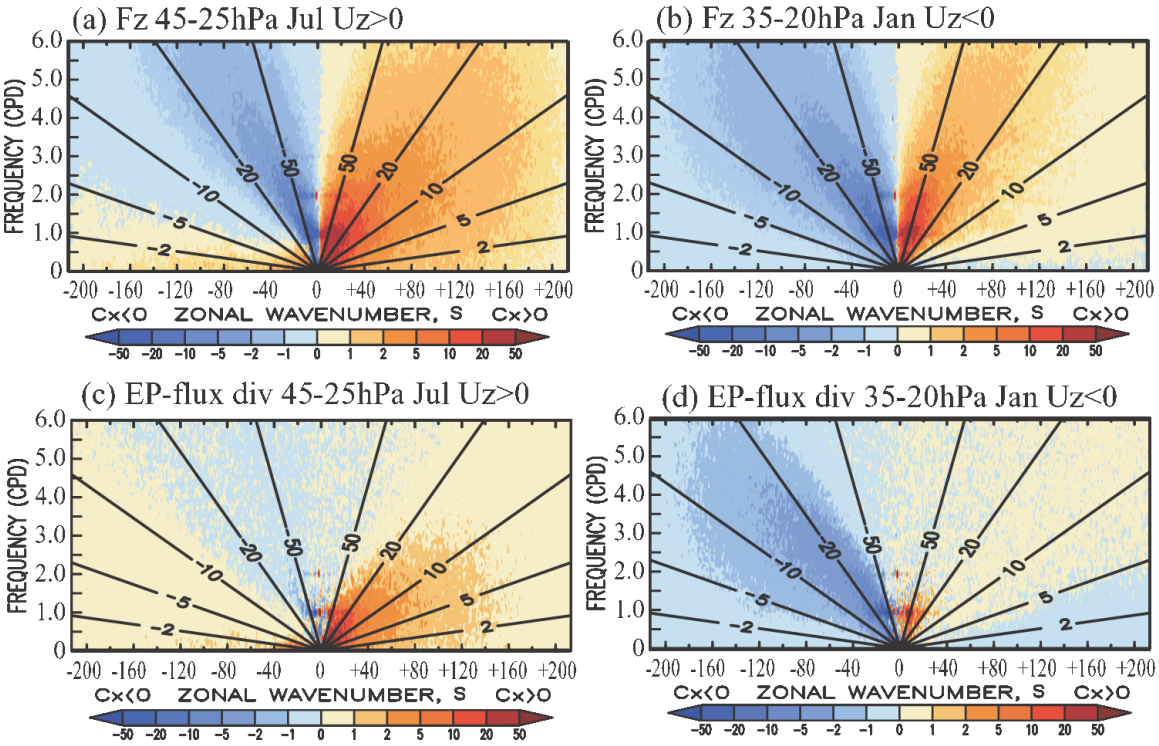

Fig. 2. Zonal wavenumber-frequency spectra of (a, b) the vertical component of EP-flux (Kg s^{-2} wavenumber^{-1} cpd^{-1}) and (c, d) EP-flux divergence (m s^{-2} wavenumber^{-1} cpd^{-1}) during (a, c) the eastward wind shear phase of the QBO in July at 45–25 hPa and (b, d) the westward wind shear phase of the QBO in January at 35–20 hPa. Solid lines show the zonal phase velocity C_x relative to the ground. Positive (negative) zonal wavenumber corresponds to positive (negative) C_x. The vertical component of EP-flux and EP-flux divergence are multiplied by 30 and 1 x 10^9, respectively. The color scale is logarithmic.

Fig. 3

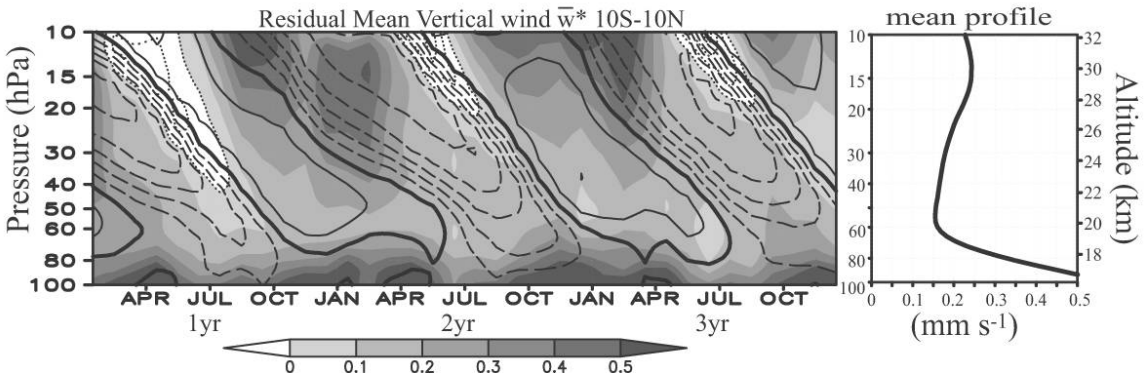

Fig. 3. Time–height cross section of the monthly mean vertical component of residual circulation $\overline{w}^*$ (white and gray shading) and zonal wind (contour) averaged from 10°N–10°S. Eastward and westward winds are represented by solid and dashed lines, respectively, with intervals of 5 m s^{-1}. Positive values are shaded and negative values are dotted, with intervals of 0.1 mm s^{-1}. Vertical profiles of averaged $\overline{w}^*$ for two cycles of the QBO are shown in the right panel with labels of log-pressure height.

Fig.4

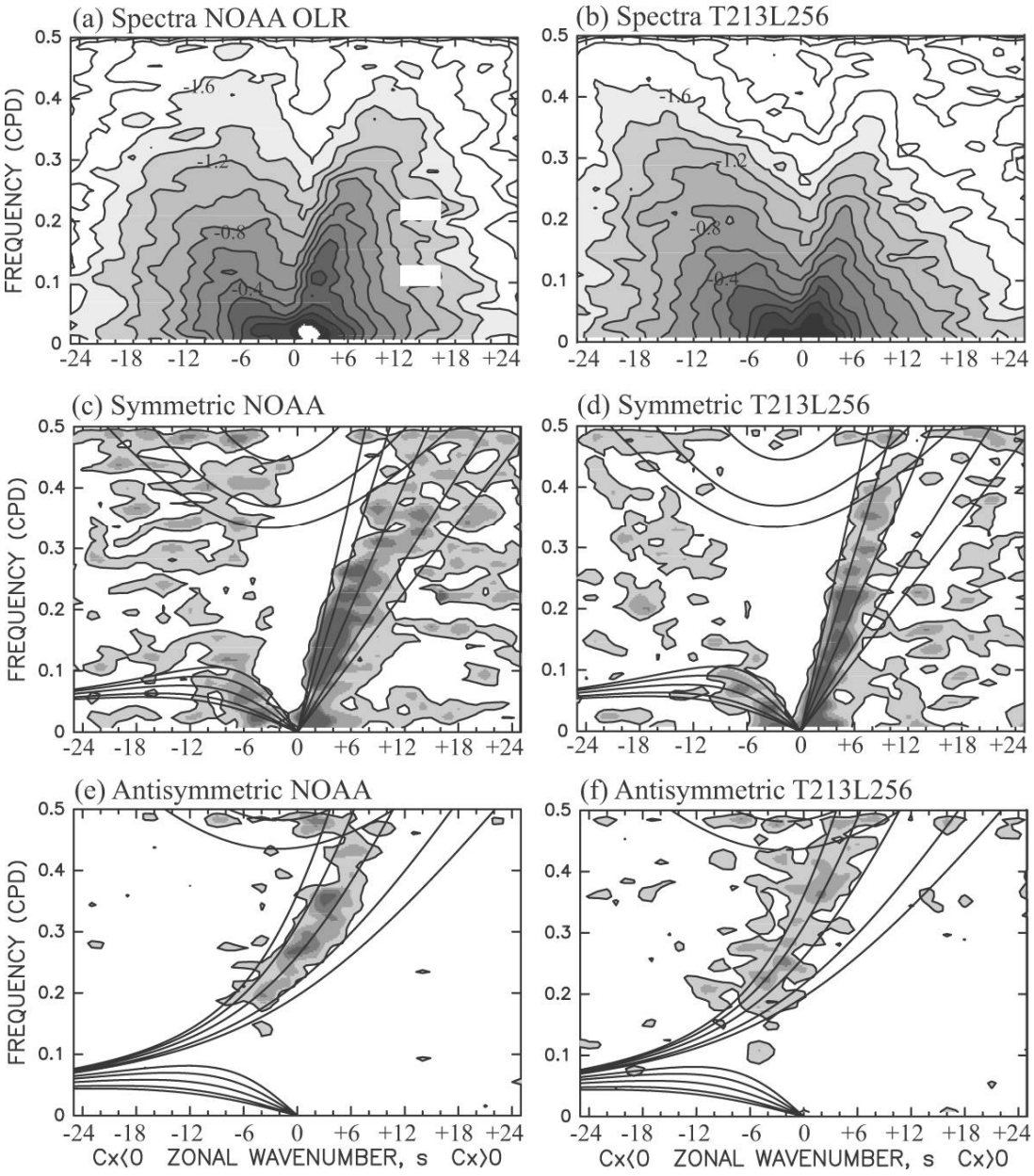

Fig. 4. (a, b) Zonal wavenumber / frequency spectra obtained by averaging the powers of symmetric and antisymmetric components of OLR averaged from 10°N to 10°S. Spectral units are $\log_{10}(W^2\ m^{-4}\ \text{wavenumber}^{-1}\ \text{cpd}^{-1})$. (c, d) Symmetric and (e, f) antisymmetric components divided by the background spectra. Left and right panels present results from NOAA OLR data and the model data, respectively. These results are from 3-year average data. The shading interval is 0.2; values ≥ 1.1 are shown for (c–f). Dispersion curves indicate the odd and even modes of equatorial waves for the five equivalent depths of 8, 12, 25, 50, and 90 m. The frequency spectral width is 1/128 cpd.

Fig.5

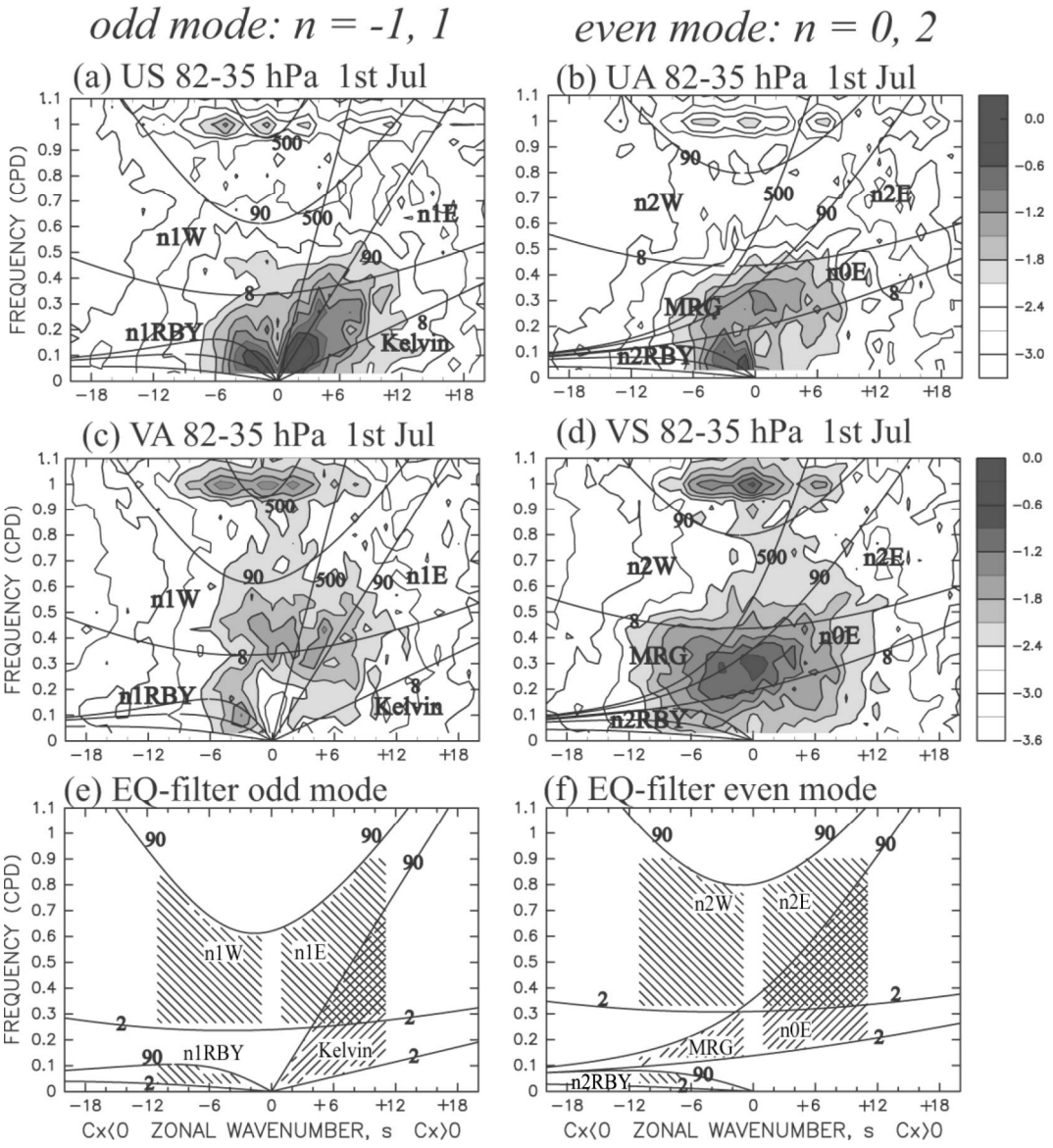

Fig. 5. Zonal wavenumber / frequency spectra of the (a, d) symmetric and (b, c) antisymmetric components of (a, b) zonal wind and (c, d) meridional wind at 82–35 hPa during July of the first year (10°N–10°S average). The spectral unit is $\log_{10}(m^2\ s^{-2}$ wavenumber^{-1} cpd^{-1}). The contour interval is 0.3 $m^2\ s^{-2}$ wavenumber^{-1} cpd^{-1}. Note that the ranges of shading differ between the zonal wind and meridional wind components; values ≥ -2.1 and ≥ -2.4 are shaded for (a, b) and (c, d), respectively. Contour lines show the dispersion curves of each EQW with equivalent depths of 8, 90, and 500 m. Application of the equatorial wave filter to (e) odd and (f) even modes of EQWs. Superposed are the dispersion curves of each EQW for two equivalent depths of 2 and 90 m. Hatched areas between the two lines are the filtering range.

Fig. 6

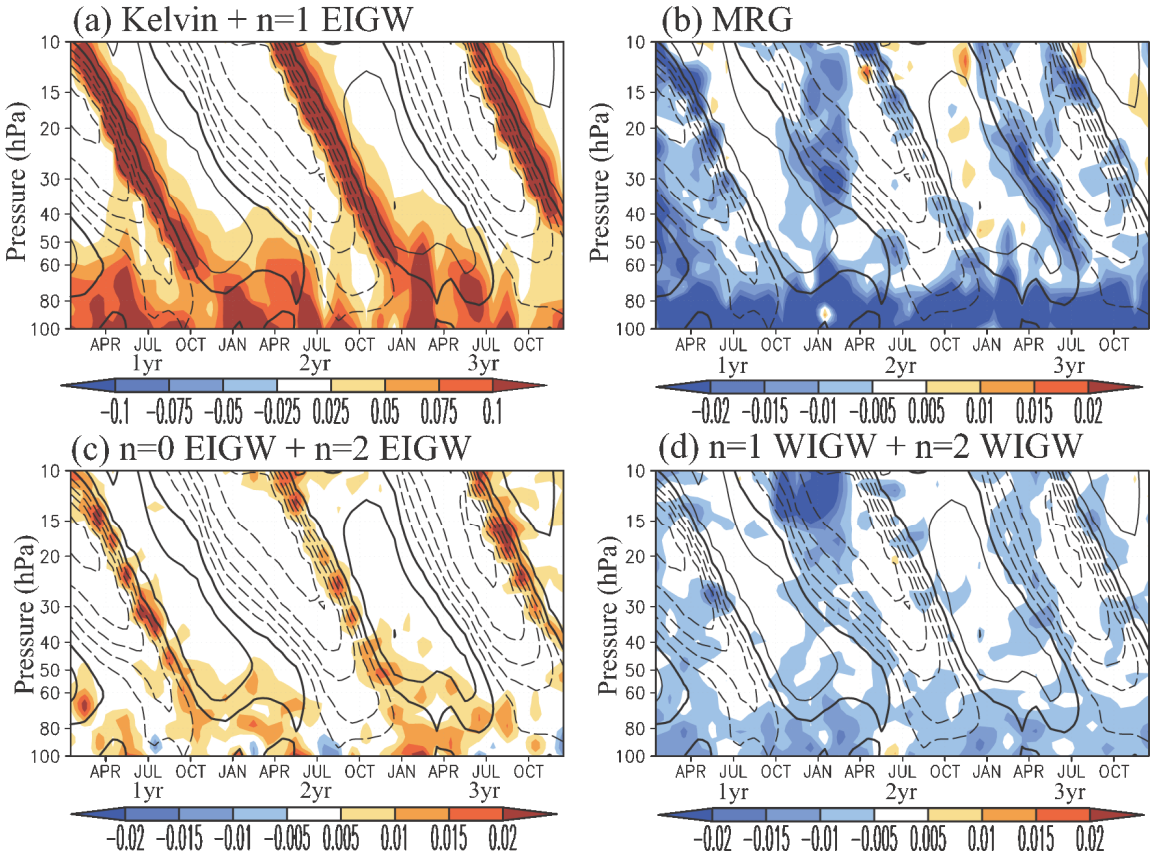

Fig. 6. Time–height cross section of monthly mean EP-flux divergence (colors) due to (a) Kelvin waves / n = 1 EIGWs, (b) MRG waves, (c) n = 0 / n = 2 EIGWs, and (d) n = 1 plus n = 2 WIGWs with equivalent depths from 2 to 90 m at 10°S–10°N. The color interval is 2.5 x 10^{-2} m s^{-1} day^{-1} for (a) and 0.5 x 10^{-2} m s^{-1} day^{-1} for (b–d). The contour interval is 5 m s^{-1} for the zonal-mean zonal wind.

Fig. 7

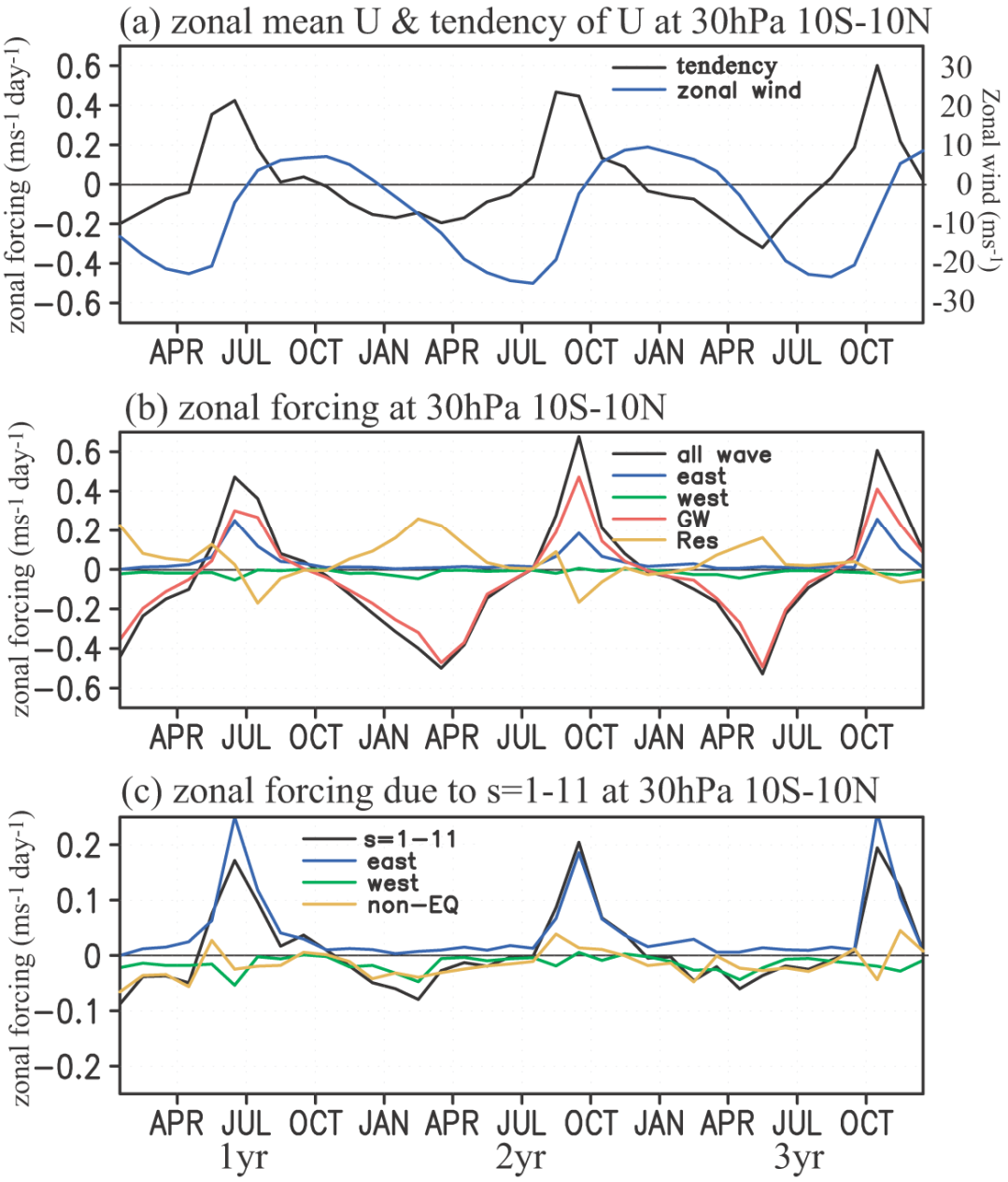

Fig. 7. Time variation of (a) zonal-mean zonal wind and its tendency; (b) monthly mean EP-flux divergence due to all waves (black), eastward EQWs (blue), westward EQWs (green), internal gravity waves (red), and forcing due to residual circulation (yellow) at 30 hPa averaged from 10°S to 10°S; (c) EP-flux divergence due to $s \leq 11$ (black), eastward EQWs (blue), westward EQWs (green), and large-scale non-EQWs (yellow), respectively. Note that the range of the ordinate axis of (c) is different from that of (a) and (b).

Fig. 8

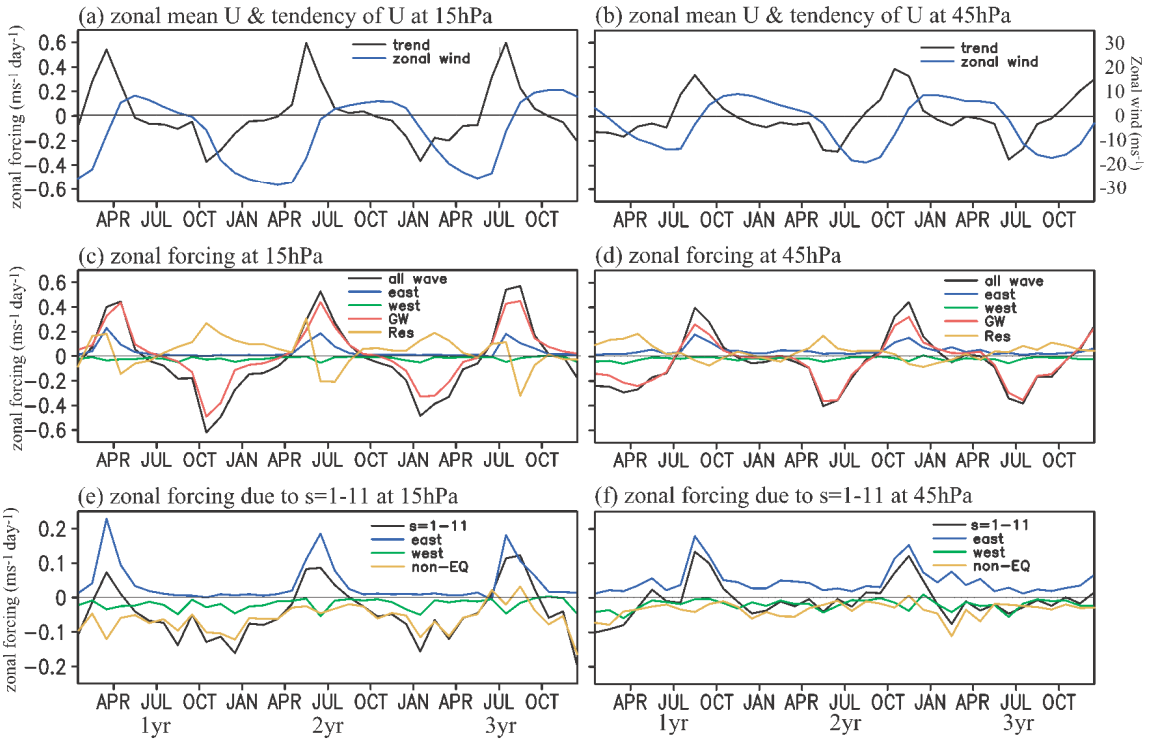

Fig.8. Same as Figure 7, but for at (a, c, e) 15 hPa and (b, d, f) 45 hPa.

Fig. 9

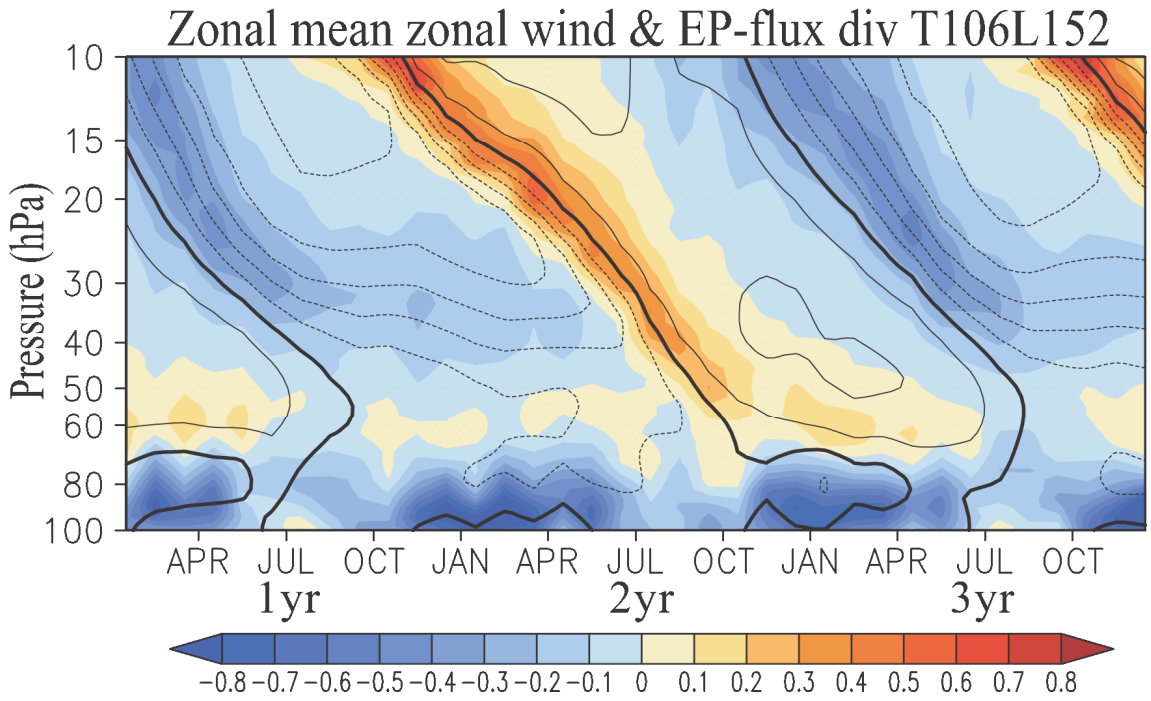

Fig. 9. Same as Figure 1a, but showing the result of the T106L152 AGCM integrated for 3 years.